

Global cracking elements: a novel tool for Galerkin-based approaches simulating quasi-brittle fracture

Yiming Zhang^{a*}, Herbert A. Mang^{b,c,d*}

^a*School of Civil and Transportation Engineering, Hebei University of Technology, Xiping Road 5340, 300401 Tianjin, P.R.China*

^b*Department of Geotechnical Engineering, Tongji University, Siping Road 1239, 200092 Shanghai, P.R.China*

^c*State Key Laboratory for Disaster Reduction in Civil Engineering, Tongji University, Siping Road 1239, 200092 Shanghai, P.R.China*

^d*Institute for Mechanics of Materials and Structures (IMWS), Vienna University of Technology, Karlsplatz 13/202, 1040 Vienna, Austria*

SUMMARY

Following the so-called Cracking Elements Method (CEM), recently presented in [1, 2], we propose a novel Galerkin-based numerical approach for simulating quasi-brittle fracture, named Global Cracking Elements Method (GCEM). For this purpose the formulation of the original CEM is reorganized. The new approach is embedded in the standard framework of the Galerkin-based Finite Element Method (FEM), which uses disconnected element-wise crack openings for capturing crack initiation and propagation. The similarity between the proposed Global Cracking Elements (GCE) and the standard 9-node quadrilateral element (Q9) suggests a special procedure: the degrees of freedom of the center node of the Q9, originally defining the displacements, are “borrowed” to describe the crack openings of the GCE. The proposed approach does not need remeshing, enrichment, or a crack-tracking strategy, and it avoids a precise description of the crack tip. Several benchmark tests provide evidence that the new approach inherits from the CEM most of the advantages. The numerical stability and robustness of the GCEM are better than the ones of the CEM. However, presently only quadrilateral elements with nonlinear interpolations of the displacement field can be used.

Copyright © 2015 John Wiley & Sons, Ltd.

Received . . .

KEY WORDS: Finite Element Method (FEM); Quasi-brittle Fracture; Standard Galerkin Form; Cracking Elements Method; Self-propagating Crack

Copyright © 2015 John Wiley & Sons, Ltd.

Prepared using nmeauth.cls [Version: 2010/05/13 v3.00]

1. INTRODUCTION

Fracture of quasi-brittle materials is accompanied by a fast strain softening process, resulting in a localized failure zone of very small size [3, 4]. In the last decades, different approaches were presented. They are made of a continuum [5, 6], discrete [7, 8] or particle/meshless [9–11] based framework, embedded either in classical fracture mechanics, or in continuum damage mechanics, or in an equivalent-type theory such as peridynamics and lattice models [12–14].

For evaluation of the ease of implementation, the reliability, robustness, and the efficiency of numerical methods for simulation of quasi-brittle fracture, the following criteria are listed in form of questions with “yes” or “no” answers:

1. Does the new method stay far outside of a conventional continuum-based framework?
2. Does it provide results that strongly depend on the discretization?
3. Does it require reprocessing such as remeshing?
4. Does it introduce extra degrees of freedom other than displacements?
5. Does it need to predict the crack path (position as well as orientation)?
6. Does it require more computing effort than a traditional FEM-based method such as the smeared-crack approach?

A good method is one with predominantly negative answers to these questions. In this paper, a novel numerical approach is presented, with “No” as the answer to all of the above questions. It is named the Global Cracking Elements Method (GCEM). Its characteristics are as follows:

1. The GCEM is developed on the basis of the original cracking elements method (CEM), presented in [1, 2, 15]. It is embedded in the conventional continuum-based framework. It may be considered as a conventional FEM approach with a special type of elements.
2. Unlike the smeared-crack approach [16], the discretization dependency of the GCEM is negligible. To demonstrate this advantage, all of the numerical examples

*Correspondence to: Herbert A. Mang and Yiming Zhang

Email: Herbert.Mang@tuwien.ac.at, Yiming.Zhang@hebut.edu.cn

in this work are characterized by irregular meshes. Besides, the mesh used in the GCEM can be relatively coarse.

3. For putting it more precisely, the GCEM is a type of Strong-Discontinuity-embedded Approach (SDA) [17–19], which obviously does not need remeshing.
4. Unlike phase field methods [20, 21], extended finite element methods (XFEM) [22, 23], or numerical manifold methods (NMM) [24–26], the GCEM does not require a precise description of the stress state at crack tips and does not need extra degrees of freedom[†].
5. Unlike the traditional SDA and the XFEM, the GCEM does not need a crack-tracking strategy [27, 28]. Disconnected element-wise cracking segments, passing through the elements, are used for representing crack paths. The orientation of the crack is determined locally, providing *self-propagating* cracks [1].
6. The global cracking elements used in the framework of the GCEM, are formally similar to the 9-node quadrilateral elements. They provide a symmetric and sparse stiffness matrix [15, 29]. Thus the numerical efficiency is reasonably high.

The main features of the GCEM are as follows:

- The designed special type of global cracking elements is formally similar to the Q9 element. The shape functions, the local stiffness matrix, and the residuals will be provided in this work.
- The domain is initially discretized by Q9 elements. Once a crack appears, the standard Q9 element will become a global cracking element by “borrowing” the displacement degrees of freedom to indicate local crack openings.
- Since the crack openings become global unknowns, the GCEM is numerically more stable and more efficient than the CEM. Fewer iteration steps than in the CEM are needed. At the same time, the self-propagating property of cracking elements is maintained.

The paper is organized as follows: In Section 2, the adopted mixed-mode softening law, the kinematics, and the designed cracking element are described. Numerical examples are presented in Section 3, including an L-shaped panel test and disk tests with initial slots.

[†]Nonetheless, a small trick is used insofar as the degrees of freedom of the center node of the Q9 are “borrowed” for indicating crack openings, see the following sections for details.

In all examples, irregular meshes, with different sizes of the elements, are used. Section 4 contains concluding remarks.

2. FORMULATION

2.1. Traction-separation law

A mixed mode traction-separation law [30, 31] is used in this work. With ζ_n and ζ_t denoting the crack openings in the normal and the parallel direction, respectively, the equivalent crack opening is defined as

$$\zeta_{eq} = \sqrt{\zeta_n^2 + \zeta_t^2}. \quad (1)$$

The traction components in the normal and the parallel direction, i.e. T_n and T_t , are obtained as

$$T_n = T_{eq} \frac{\zeta_n}{\zeta_{eq}}, \quad T_t = T_{eq} \frac{\zeta_t}{\zeta_{eq}}$$

with

$$T_{eq}(\zeta_{eq}) = \begin{cases} L_1(\zeta_{eq}) = \frac{f_t}{\zeta_0} \zeta_{eq}, & \text{loading, } \zeta_{eq} \leq \zeta_0 \\ L_2(\zeta_{eq}) = f_t \exp\left[-\frac{f_t(\zeta_{eq} - \zeta_0)}{G_f - G_{f,0}}\right], & \text{loading, } \zeta_{eq} > \zeta_0 \\ U(\zeta_{eq}) = \frac{T_{mx}}{\zeta_{mx}} \zeta_{eq}, & \text{unloading/reloading,} \end{cases} \quad (2)$$

where f_t is the uniaxial tensile strength, G_f is the fracture energy, $G_{f,0}$ is the threshold value of G_f , with $G_{f,0} = 0.001 G_f$ assumed herein, ζ_0 is the threshold opening, given as $\zeta_0 = 2 G_{f,0}/f_t$, and ζ_{mx} denotes the maximum opening, which the crack has ever experienced. Its value is updated at the end of every loading step if $\zeta_{mx} > \zeta_0$. $T_{mx} = L_2(\zeta_{mx})$ is the corresponding traction. Figure 1 shows $T_{eq}(\zeta_{eq})$.

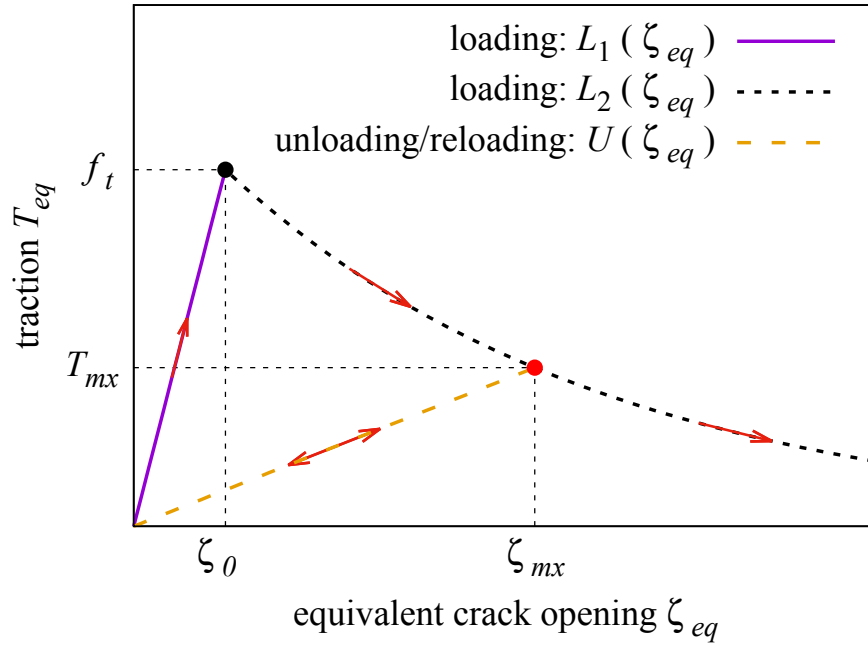


Figure 1: Traction-separation curve $T_{eq}(\zeta_{eq})$

From equations 1 and 2, the following relations can be obtained

$$\mathbf{D} = \begin{bmatrix} \partial T_n / \partial \zeta_n & \partial T_n / \partial \zeta_t \\ \partial T_t / \partial \zeta_n & \partial T_t / \partial \zeta_t \end{bmatrix} = \begin{cases} \frac{f_t}{\zeta_0} \begin{bmatrix} 1 & 0 \\ 0 & 1 \end{bmatrix}, & \text{loading, } \zeta_{eq} \leq \zeta_0 \\ -\frac{T_{eq}}{\zeta_{eq}^2} \begin{bmatrix} \frac{\zeta_n^2}{\zeta_{eq}} + \frac{f_t \zeta_n^2}{G_f - G_{f,0}} - \zeta_{eq} & \frac{\zeta_n \zeta_t}{\zeta_{eq}} + \frac{f_t \zeta_n \zeta_t}{G_f - G_{f,0}} \\ \frac{\zeta_n \zeta_t}{\zeta_{eq}} + \frac{f_t \zeta_n \zeta_t}{G_f - G_{f,0}} & \frac{\zeta_t^2}{\zeta_{eq}} + \frac{f_t \zeta_t^2}{G_f - G_{f,0}} - \zeta_{eq} \end{bmatrix}, & \text{loading, } \zeta_{eq} > \zeta_0 \\ \frac{T_{mx}}{\zeta_{mx}} \begin{bmatrix} 1 & 0 \\ 0 & 1 \end{bmatrix}, & \text{unloading/reloading.} \end{cases} \quad (3)$$

These relations will be used for computation of the stiffness matrix and the residual of the cracking element.

2.2. Kinematics

The deduction of the displacement field $\mathbf{u}(\mathbf{x})$ and of the corresponding strain field $\boldsymbol{\varepsilon}(\mathbf{x})$ of the cracking element can be found in [1, 15]. The result for $\mathbf{u}(\mathbf{x})$ is given as

$$\mathbf{u}(\mathbf{x}) = \bar{\mathbf{u}}(\mathbf{x}) + [H_s(\mathbf{x}) - \varphi(\mathbf{x})][[u]], \quad (4)$$

where $\bar{\mathbf{u}}(\mathbf{x})$ is the regular part, $H_s(\mathbf{x})$ is the Heaviside function across the discontinuity surface, with $H_s(\mathbf{x}) = 1$ on one side of the subdomain and $H_s(\mathbf{x}) = 0$ on the other side, and $\varphi(\mathbf{x})$ is a differentiable function with $\varphi(\mathbf{x}) \in [0, 1]$. The result for $\bar{\boldsymbol{\varepsilon}}(\mathbf{x})$ is obtained as

$$\bar{\boldsymbol{\varepsilon}}(\mathbf{x}) = \underbrace{\nabla^S \bar{\mathbf{u}}(\mathbf{x})}_{\text{total strain } \hat{\boldsymbol{\varepsilon}}} - \underbrace{[(\mathbf{n} \otimes \nabla \varphi)^S \zeta_n(\mathbf{x}) + (\mathbf{t} \otimes \nabla \varphi)^S \zeta_t(\mathbf{x})]}_{\text{enhanced strain } \tilde{\boldsymbol{\varepsilon}}}, \quad (5)$$

where, unit vectors corresponding to ζ_n and ζ_t are denoted as \mathbf{n} and \mathbf{t} , respectively. In the presented symmetric formulation[‡], $\nabla \varphi \parallel \mathbf{n}$. Then, based on energy conservation [15], $\nabla \varphi = \mathbf{n} / l_c$ is obtained, with $l_c = V/A$. In this formula, V is the volume of the cracking element and A is the area of an equivalent crack surface, i.e. the surface of a parallel crack, passing through the center point of the element, as shown in Figure 2. Hereby, l_c corresponds to the classical characteristic length. It only depends on the shape of the element and on the orientation of the crack, but not on its position.

For the FEM approximation of the 8-node quadrilateral element (Q8), Eq. 5 is obtained as

$$\bar{\boldsymbol{\varepsilon}}^{(e)} \approx \underbrace{\sum_{i=1}^8 \left(\nabla N_i^{(e)} \otimes \mathbf{u}_i \right)^S}_{\hat{\boldsymbol{\varepsilon}}^{(e)}} - \underbrace{\frac{1}{l_c^{(e)}} \left[(\mathbf{n}^{(e)} \otimes \mathbf{n}^{(e)}) \zeta_n^{(e)} + (\mathbf{n}^{(e)} \otimes \mathbf{t}^{(e)})^S \zeta_t^{(e)} \right]}_{\tilde{\boldsymbol{\varepsilon}}^{(e)}}, \quad (6)$$

where $(\cdot)^S$ denotes the symmetric part of the tensor [32] and $(\cdot)^{(e)}$ is the value of the respective quantity of the Q8 element e . E.g., $N_i^{(e)}$ is a shape function.

Furthermore, in [1, 2, 15] an idea referred to as “*center representation*”, is presented. Once a crack appears in an element, the stress/strain state at the center Gauss point is

[‡]In this approach $\varphi(\mathbf{x})$ does not have to be known, while in the XFEM and in some other types of SDA $\varphi(\mathbf{x}) = \sum N_i \varphi_i$ is assumed. Therefore, the proposed approach is easier to implement, and it has fewer assumptions.

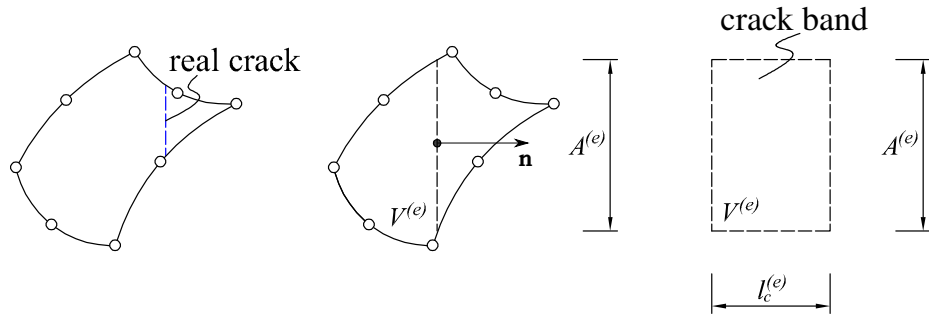


Figure 2: Determination of the value of l_c of element e , with the volume $V^{(e)}$ and the effective cracking area $A^{(e)}$ (based on a parallel crack passing through the center point)

used for representation of the stress/strain state of the whole element. Considering the equivalence of forces of discrete and embedded models [15], the following relations exist not just at the center point, but in the whole cracking element:

$$\begin{aligned} \boldsymbol{\sigma}^{(e)} &= \mathbb{C}^{(e)} : \bar{\boldsymbol{\varepsilon}}^{(e)} \quad \text{and} \\ \left\{ \begin{array}{l} (\mathbf{n}^{(e)} \otimes \mathbf{n}^{(e)}) : \boldsymbol{\sigma}^{(e)} - T_n^{(e)} = 0 \\ (\mathbf{n}^{(e)} \otimes \mathbf{t}^{(e)})^S : \boldsymbol{\sigma}^{(e)} - T_t^{(e)} = 0 \end{array} \right. , \end{aligned} \quad (7)$$

where $\mathbb{C}^{(e)}$ is the elasticity tensor.

2.3. Global Cracking Element

In this subsection, the Voigt notation is used for representation of second- and fourth-order tensors with corresponding vector and matrix forms [33]. For the Q8 element, the displacement vector is given as $\mathbf{U}^{(e)} = [\mathbf{u}_1^{(e)} \cdots \mathbf{u}_8^{(e)}]^T$. The \mathbf{B} matrix is given as

$$\mathbf{B}^{(e)} = \left[\mathbf{B}_1^{(e)} \quad \cdots \quad \mathbf{B}_8^{(e)} \right],$$

where

$$\mathbf{B}_i^{(e)} = \begin{bmatrix} \frac{\partial N_i^{(e)}}{\partial x} & 0 \\ 0 & \frac{\partial N_i^{(e)}}{\partial y} \\ \frac{\partial N_i^{(e)}}{\partial y} & \frac{\partial N_i^{(e)}}{\partial x} \end{bmatrix}, \quad i = 1 \cdots 8. \quad (8)$$

The unit vectors $\mathbf{n}^{(e)}$ and $\mathbf{t}^{(e)}$ are given as $\mathbf{n}^{(e)} = [n_x^{(e)}, n_y^{(e)}]^T$ and $\mathbf{t}^{(e)} = [t_x^{(e)}, t_y^{(e)}]^T$. Then, based on Eq. 6, a special matrix $\mathbf{B}_\zeta^{(e)}$ is introduced as follows:

$$\mathbf{B}_\zeta^{(e)} = \frac{-1}{l_c^{(e)}} \begin{bmatrix} \mathbf{n}^{(e)} \otimes \mathbf{n}^{(e)} \\ (\mathbf{n}^{(e)} \otimes \mathbf{t}^{(e)})^S \end{bmatrix}^T = \frac{-1}{l_c^{(e)}} \begin{bmatrix} n_x^{(e)} \cdot n_x^{(e)} & n_x^{(e)} \cdot t_x^{(e)} \\ n_y^{(e)} \cdot n_y^{(e)} & n_y^{(e)} \cdot t_y^{(e)} \\ 2 n_x^{(e)} \cdot n_y^{(e)} & n_x \cdot t_y^{(e)} + n_y^{(e)} \cdot t_x^{(e)} \end{bmatrix}. \quad (9)$$

Thus, $\tilde{\boldsymbol{\varepsilon}}^{(e)} = -\mathbf{B}_\zeta^{(e)} \boldsymbol{\zeta}^{(e)}$, where $\boldsymbol{\zeta}^{(e)} = [\zeta_n^{(e)} \ \zeta_t^{(e)}]^T$. With $\mathbf{B}_\zeta^{(e)}$, Eq. 7 can be rewritten as follows:

$$-l_c \left(\mathbf{B}_\zeta^{(e)} \right)^T \boldsymbol{\sigma}^{(e)} - \begin{bmatrix} T_n^{(e)} \\ T_t^{(e)} \end{bmatrix} = \mathbf{0}. \quad (10)$$

Next, for convenience we assume that $\mathbf{B}^{(e),1}$ denotes $\mathbf{B}^{(e)}$ for the center Gauss point. Thus, Eq. 6 gives

$$\tilde{\boldsymbol{\varepsilon}}^{(e)} = \tilde{\boldsymbol{\varepsilon}}^{(e),1} = \begin{bmatrix} \mathbf{B}^{(e),1} & \mathbf{B}_\zeta^{(e)} \end{bmatrix} \begin{bmatrix} \mathbf{U}^{(e)} \\ \boldsymbol{\zeta}^{(e)} \end{bmatrix}. \quad (11)$$

The elastic energy $E^{(e)}$ is obtained as

$$E^{(e)} = \frac{1}{2} \int \boldsymbol{\sigma}^e \cdot \tilde{\boldsymbol{\varepsilon}}^{(e)} d(e) = \frac{V^{(e)}}{2} \left(\tilde{\boldsymbol{\varepsilon}}^{(e)} \right)^T \mathbf{C}^{(e)} \tilde{\boldsymbol{\varepsilon}}^{(e)}, \quad (12)$$

where $\int(\cdot)d(e)$ is the integral of $\boldsymbol{\sigma}^e \cdot \tilde{\boldsymbol{\varepsilon}}^{(e)}$ in the element e and \mathbf{C}^e denotes the matrix form of $\mathbb{C}^{(e)}$. The elastic energy is used for checking whether the equilibrium iteration by means of the Newton-Raphson (N-R) method converges, see the next section for the details.

For the iteration step l within load step i in the framework of the N-R iteration [1, 31], the following relation is obtained:

$$\begin{bmatrix} \mathbf{U}_{i,l}^{(e)} \\ \boldsymbol{\zeta}_{i,l}^{(e)} \end{bmatrix} = \underbrace{\begin{bmatrix} \mathbf{U}_{i-1}^{(e)} \\ \boldsymbol{\zeta}_{i-1}^{(e)} \end{bmatrix} + \begin{bmatrix} \Delta \mathbf{U}_{l-1}^{(e)} \\ \Delta \boldsymbol{\zeta}_{l-1}^{(e)} \end{bmatrix}}_{\text{known}} + \underbrace{\begin{bmatrix} \Delta \Delta \mathbf{U}^{(e)} \\ \Delta \Delta \boldsymbol{\zeta}^{(e)} \end{bmatrix}}_{\text{unknown}}, \quad (13)$$

where $\Delta(\cdot)$ denotes an increment with respect to the corresponding value at the preceding load step, $i - 1$, and $\Delta\Delta(\cdot)$ stands for an increment with respect to the value at the last N-R iteration step, $l - 1$. The N-R iteration process was described in [2].

The balance equation $\nabla\sigma = \mathbf{F}$ for quasi-static loading, where \mathbf{F} denotes the loading force, and making use of the equivalence relations according to Eq. 10, after linearization the global balance equation is obtained as follows:

$$\mathbf{K}_s^{(e)} \begin{bmatrix} \Delta\Delta\mathbf{U} \\ \Delta\Delta\zeta \end{bmatrix} = \begin{bmatrix} \mathbf{F} \\ \mathbf{T} \end{bmatrix} - \mathbf{K}^{(e)} \begin{bmatrix} \mathbf{U}_{i-1}^{(e)} + \Delta\mathbf{U}_{l-1}^{(e)} \\ \zeta_{i-1}^{(e)} + \Delta\zeta_{l-1}^{(e)} \end{bmatrix},$$

with

$$\mathbf{K}^{(e)} = \begin{bmatrix} \int (\mathbf{B}^{(e)})^T \mathbf{C}^e (\mathbf{B}^{(e),1}) d(e) & \int (\mathbf{B}^{(e)})^T \mathbf{C}^e \mathbf{B}_\zeta^{(e)} d(e) \\ -l_c (\mathbf{B}_\zeta^{(e)})^T \mathbf{C}^e (\mathbf{B}^{(e),1}) & -l_c (\mathbf{B}_\zeta^{(e)})^T \mathbf{C}^e \mathbf{B}_\zeta^{(e)} \end{bmatrix} \quad (14)$$

and

$$\mathbf{K}_s^{(e)} = \mathbf{K}^{(e)} - \begin{bmatrix} \mathbf{0} & \mathbf{0} \\ \mathbf{0} & \mathbf{D}^{(e)} \end{bmatrix},$$

where, $\mathbf{T} = \mathbf{T}(\zeta_{i-1}^{(e)} + \Delta\zeta_{l-1}^{(e)}) = [T_n \ T_t]^T$. Eq. 14 is not useful for numerical analysis, because neither $\mathbf{K}_s^{(e)}$ nor $\mathbf{K}^{(e)}$ is symmetric. As a remedy of this problem, Eq. 14 is slightly changed to

$$\mathbf{K}_{s,new}^{(e)} \begin{bmatrix} \Delta\Delta\mathbf{U} \\ \Delta\Delta\zeta \end{bmatrix} = \begin{bmatrix} \mathbf{F} \\ -V^{(e)} / l_c^{(e)} \mathbf{T} \end{bmatrix} - \mathbf{K}_{new}^{(e)} \begin{bmatrix} \mathbf{U}_{i-1}^{(e)} + \Delta\mathbf{U}_{l-1}^{(e)} \\ \zeta_{i-1}^{(e)} + \Delta\zeta_{l-1}^{(e)} \end{bmatrix},$$

with

$$\mathbf{K}_{new}^{(e)} = \begin{bmatrix} \int (\mathbf{B}^{(e)})^T \mathbf{C}^e (\mathbf{B}^{(e),1}) d(e) & \int (\mathbf{B}^{(e)})^T \mathbf{C}^e \mathbf{B}_\zeta^{(e)} d(e) \\ V^{(e)} (\mathbf{B}_\zeta^{(e)})^T \mathbf{C}^e (\mathbf{B}^{(e),1}) & V^{(e)} (\mathbf{B}_\zeta^{(e)})^T \mathbf{C}^e \mathbf{B}_\zeta^{(e)} \end{bmatrix} \quad (15)$$

and

$$\mathbf{K}_{s,new}^{(e)} = \mathbf{K}_{new}^{(e)} + \begin{bmatrix} \mathbf{0} & \mathbf{0} \\ \mathbf{0} & V^{(e)} / l_c \mathbf{D}^{(e)} \end{bmatrix}.$$

However, also $\mathbf{K}_{s,new}^{(e)}$ is not symmetric. Moreover, this matrix has many zero elements, rendering the iteration numerically unstable. Fortunately, $\mathbf{K}_{s,new}^{(e)}$ can be replaced by the

following symmetric matrix:

$$\mathbf{K}_{sym}^{(e)} = \int \left[\mathbf{B}^{(e)} \quad \mathbf{B}_{\zeta}^{(e)} \right]^T \mathbf{C}^e \left[\mathbf{B}^{(e)} \quad \mathbf{B}_{\zeta}^{(e)} \right] d(e) + \begin{bmatrix} \mathbf{0} & \mathbf{0} \\ \mathbf{0} & V^{(e)} / l_c \mathbf{D}^{(e)} \end{bmatrix}. \quad (16)$$

It is worth mentioning that the matrix $\mathbf{K}_{new}^{(e)}$, see Eq. 15, appearing as the final term on the right-hand side of Eq. 15 remains the same. Otherwise serious stress locking would occur (see Appendix A of [15]).

Finally, the nodal displacement vector $\mathbf{U}_{pseudo-Q9}^{(e)}$ and the matrix $\mathbf{B}_{pseudo-Q9}^{(e)}$ are defined as follows:

$$\mathbf{U}_{pseudo-Q9}^{(e)} = \begin{bmatrix} \mathbf{U}^{(e)} \\ \zeta^{(e)} \end{bmatrix}, \quad \mathbf{B}_{pseudo-Q9}^{(e)} = \left[\mathbf{B}^{(e)} \quad \mathbf{B}_{\zeta}^{(e)} \right]. \quad (17)$$

They are similar to the displacement vector and the \mathbf{B} matrix of the Q9 element. The original displacement of the center node of this element has been replaced by the element-wise crack openings $\zeta_n^{(e)}$ and $\zeta_t^{(e)}$.

By introducing $\Delta\Delta\zeta^{(e)}$ as a global unknown quantity, the relationship between $\Delta\Delta\mathbf{U}^{(e)}$ and $\Delta\Delta\zeta^{(e)}$ is established with the help of Eq. 15. As compared to the CEM, where $\zeta_{i-1}^{(e)} + \Delta\zeta_{l-1}^{(e)}$ is obtained from $\mathbf{U}_{i-1}^{(e)} + \Delta\mathbf{U}_{l-1}^{(e)}$ by an additional iteration on the element level, the N-R iteration in the framework of the GCEM is more efficient, because fewer iteration steps are needed. This will be verified in the numerical investigation.

In summary, the formulation of the cracking element, presented in [1], is converted to matrix form, resulting in a pseudo-Q9 formulation. With this in mind, the presented formulation can easily be changed to an enriched form of the crack opening [34]. In other words, the extra degrees of freedom for indicating crack openings are only introduced if cracks appear.

2.4. Initiation and propagation of cracks

The local criterion, presented in [1], is used for determining the orientation $\mathbf{n}^{(e)}$ of the crack as

$$\hat{\boldsymbol{\varepsilon}}^{(e)} \cdot \mathbf{n}^{(e)} - \hat{\boldsymbol{\varepsilon}}_1^{(e)} \cdot \mathbf{n}^{(e)} = \mathbf{0}, \quad (18)$$

where $\widehat{\boldsymbol{\varepsilon}}^{(e)} = \sum_{i=1}^8 \left(\nabla N_i^{(e)} \otimes \mathbf{u}_i \right)^S$ and $\widehat{\varepsilon}_1^{(e)}$ is the first eigenvalue of $\widehat{\boldsymbol{\varepsilon}}^{(e)}$, i.e., $\mathbf{n}^{(e)}$ coincides with the unit eigenvector corresponding to $\widehat{\varepsilon}_1^{(e)}$ [§]. For 2D analysis, with

$$\widehat{\boldsymbol{\varepsilon}}^{(e)} = \begin{bmatrix} \widehat{\varepsilon}_x^{(e)} & \widehat{\gamma}_{xy}^{(e)} / 2 \\ \widehat{\gamma}_{xy}^{(e)} / 2 & \widehat{\varepsilon}_y^{(e)} \end{bmatrix}, \quad (19)$$

$\widehat{\varepsilon}_1^{(e)}$ is obtained as

$$\widehat{\varepsilon}_1^{(e)} = \frac{\widehat{\varepsilon}_x^{(e)} + \widehat{\varepsilon}_y^{(e)} + \sqrt{\left(\widehat{\varepsilon}_x^{(e)} - \widehat{\varepsilon}_y^{(e)} \right)^2 + \left(\widehat{\gamma}_{xy}^{(e)} \right)^2}}{2}, \quad (20)$$

which permits determination of $\mathbf{n}^{(e)}$ based on Eq. 18.

One disadvantage of Eq. 18 is that $\mathbf{n}^{(e)}$ rotates during loading. This is even the case within one loading step if, e.g., a new crack appears. However, since $\mathbf{n}^{(e)}$ depends on $\widehat{\boldsymbol{\varepsilon}}^{(e)}$ but not $\bar{\boldsymbol{\varepsilon}}^{(e)}$, this rotation is very small.

Similar to the procedure described in [1], the uncracked elements of the domain are separated into two regions: the propagation region and the new root-search region. This is done with a simple criterion, checking whether the element shares at least one boundary with a cracking element, see Figure 3. The following strategy is used to find the next cracking element:

$$\begin{aligned} & \text{find } \max \left\{ \phi_{RK}^{(e)} \right\}, \text{ with} \\ & \phi_{RK}^{(e)} = \left(\mathbf{n}^{(e)} \otimes \mathbf{n}^{(e)} \right) : \mathbb{C}^{(e)} : \widehat{\boldsymbol{\varepsilon}}^{(e)} - f_t^{(e)} \\ & \text{and } \phi_{RK}^{(e)} > 0, \end{aligned} \quad (21)$$

where the propagation region is always at first searched for the existence of a propagation region[¶]. If a new cracking element appears in the propagation region, this region will consequently expand, and the search will be continued. If no new cracking element is found in the propagation region, the new root-search region will be checked. If that a new cracking element appears in the new root-search region, the propagation region will

[§]Using the Voigt notation, $\widehat{\boldsymbol{\varepsilon}}^{(e)} = \mathbf{B}^{(e),1} \mathbf{U}^{(e)}$ is obtained. However, $\widehat{\boldsymbol{\varepsilon}}^{(e)}$ in Eq. 18 is written in matrix form.

[¶]For a domain without cracks, a propagation region obviously does not exist. Thus, the whole domain belongs to the new root-search region.

further expand and the search in the propagation region will again be continued. If still no new cracking element is found in the new root-search region, the next loading step will start. With this strategy, both the initiation and the propagation of cracks can be captured.

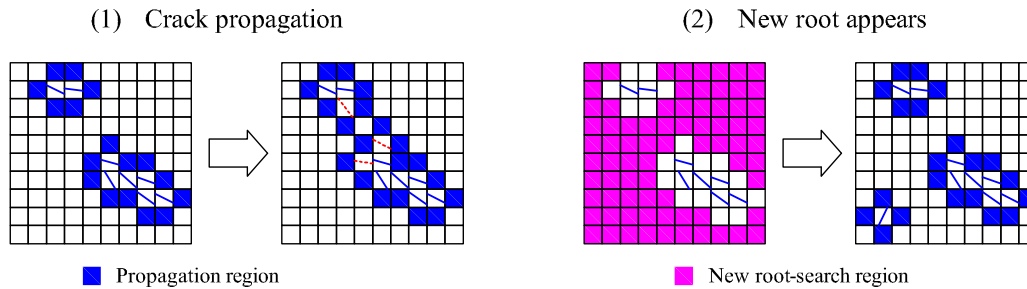


Figure 3: Separation of the uncracked elements into the propagation region and the new root-search region. If a new cracking element appears, the propagation region will expand.

The algorithm of the described procedure is illustrated in Figure 4. The procedure is simpler than the one used in the framework of the CEM [1]. The domain is firstly discretized by Q9 elements. Once a new crack appears, the standard Q9 element is converted to a pseudo-Q9 cracking element, as described in the previous section.

As mentioned before, the degrees of freedom of the center node of the Q9 element are “borrowed” for indicating element-wise crack openings. Therefore, at least theoretically these degrees of freedom can be returned. However, the criterion is very strict insofar as only in case of $\zeta_{eq}^{(e)} = 0$ and if the cracking element is not neighbor of any other cracking elements, the mentioned degrees of freedom will be returned to the center node, indicating its displacement. In all of our numerical examples, no degrees of freedom were returned. In other words, in all of the numerical examples the transformation from the standard Q9 to the pseudo-Q9 cracking element was never followed by its reversal.

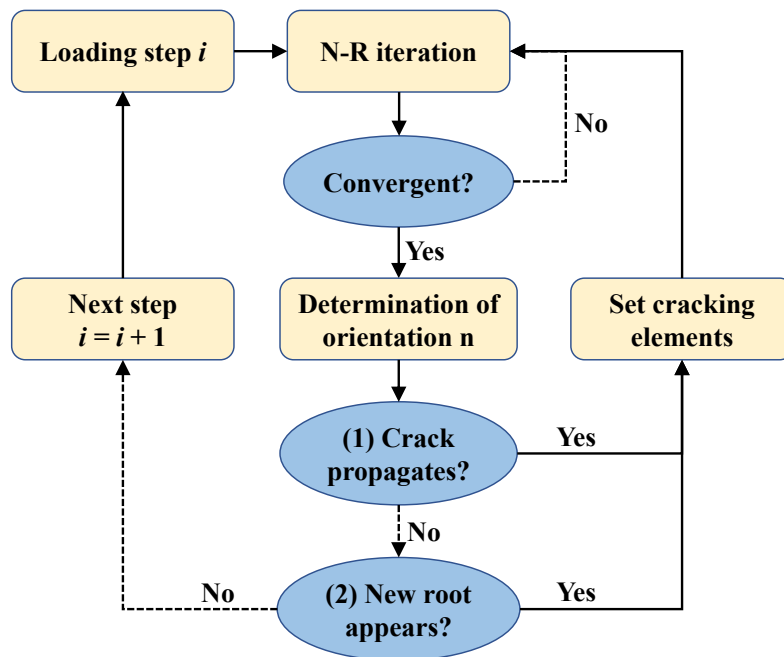


Figure 4: Calculation procedure within one N-R iteration step

3. NUMERICAL EXAMPLES

Plane-stress assumptions hold for all the numerical examples presented in this section.

3.1. L-shaped panel

The L-shaped panel test, investigated in this paper, was studied before in [1, 15]. The set-up and the material parameters are shown in Figure 5. The displacement increment is chosen as $\Delta d = 10 \mu\text{m}$. The meshes considered in this work are shown in Figure 6.

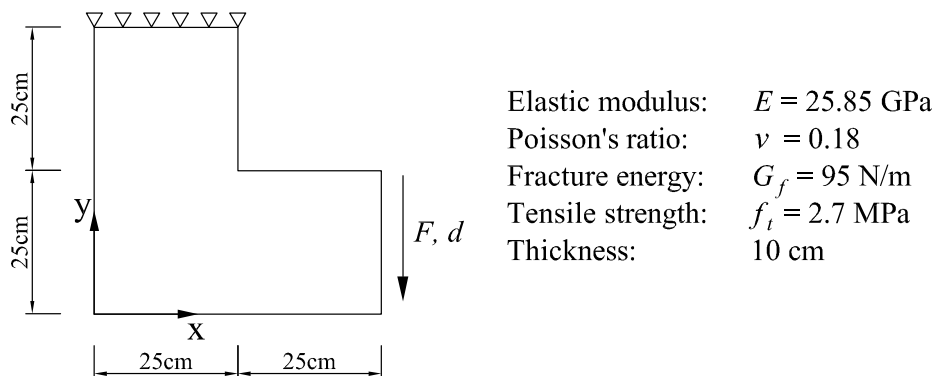


Figure 5: Set-up and material parameters of L-shaped panel test

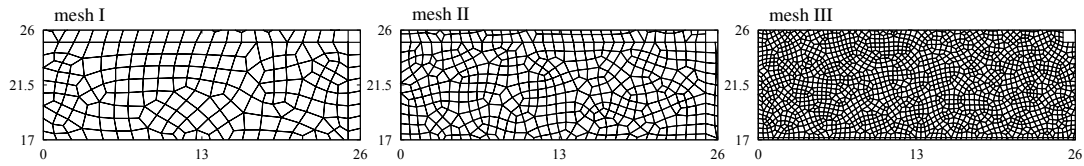


Figure 6: Meshes for the L-shaped panel test (unit: cm)

Force-displacement curves are shown in Figure 7, indicating good agreement with the results obtained by the XFEM [30] and by the CEM. In the calculations, the total elastic energy, given in Eq.12, was used for checking whether the iteration converges. Thus, if

$$\text{if } \left| \frac{\sum_e E_l^{(e)} - \sum_e E_{l-1}^{(e)}}{\sum_e E_l^{(e)}} \right| < 10^{-5}, \quad (22)$$

then the N-R iteration converged at step l for the CEM and the GCEM. The numbers of the N-R iterations are shown in Figure 8. It is seen that the GCEM needs fewer iterations than the CEM. Deformation and crack-opening plots are shown in Figures 9 and 10. The obtained results for mixed mode crack openings, for different meshes, compare well with each other.

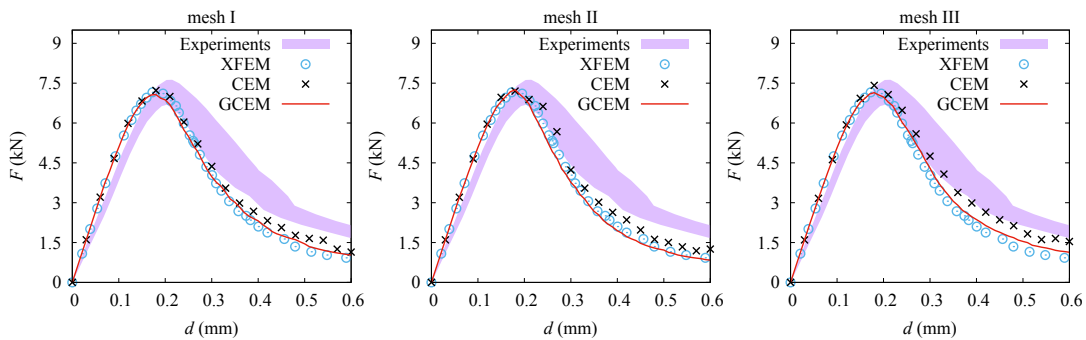


Figure 7: Force-displacement curves of the L-shaped panel for different meshes, comparing the results for the GCEM to the experimental results [35] and the results obtained by the XFEM [30] and by the CEM [1]

3.2. Brazilian disk tests with single or double slots

Brazilian disk tests with single or double slots were studied experimentally in [36]. Numerical simulations were conducted by the phase field method [37], the peridynamics theory [38], and by the lattice element model [39]. Similar to the GCEM, these methods

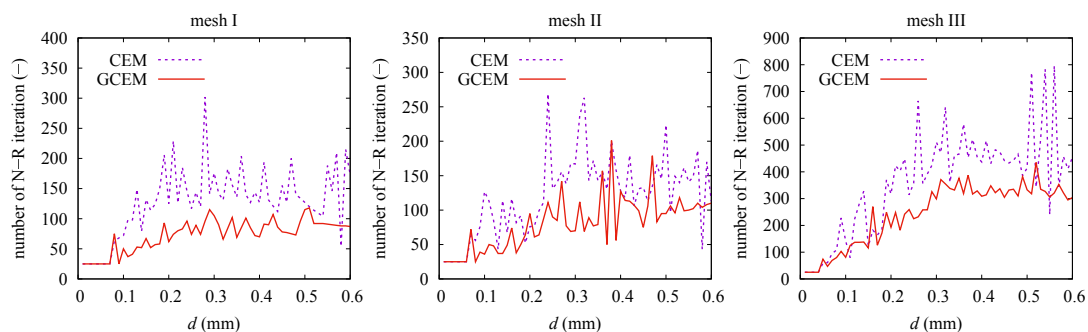


Figure 8: Comparison of the number of iterations for the GCEM with the one for the CEM

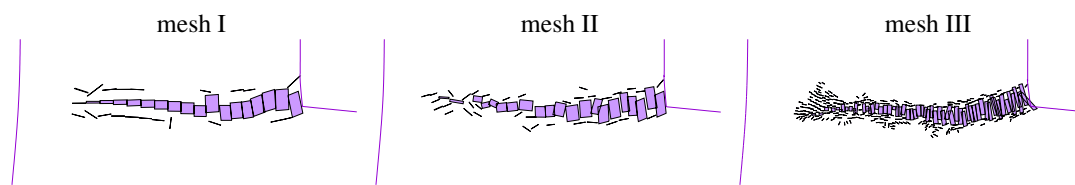


Figure 9: Deformation and crack-opening plots of the L-shaped panel, for $d = 450 \mu\text{m}$ (scale=1:100)

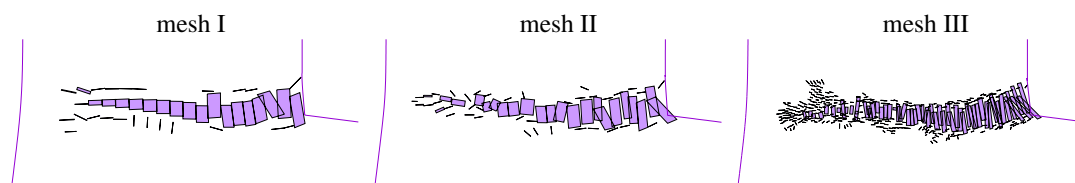


Figure 10: Deformation and crack-opening plots of the L-shaped panel, for $d = 600 \mu\text{m}$ (scale=1:100)

do not need crack tracking. However, it will be shown that in case of the GCEM, good results are obtained with coarser meshes.

The models of the tests are shown in Figure 11. The slot width is chosen as 1 mm. The displacement increment is chosen as $\Delta d = 0.5 \mu\text{m}$. The meshes are shown in Figure 12. They change slightly with different analysis of inclination, α , of the crack. For simulations of disk tests with a single slot, coarse as well as fine meshes are considered, whereas only fine meshes are used for simulating disk tests with double slots. For intact disks, the relationship between the ultimate loading per unit thickness, F_{max} , and the tensile strength f_t is given as

$$F_{max} = \frac{\pi D f_t}{2} = 598.47 \text{ kN}, \quad (23)$$

which is used for determination of normalized peak loads.

For disk tests with a single slot, the force-displacement curves are shown for different meshes in Figure 13, indicating similar peak loads and load histories. The normalized peak loads are shown in Figure 14 for the GCEM, the phase field method [38] and the peridynamics theory [38]. The results provide evidence of the reliability of GCEM. The mesh dependency is very small. The results of the crack openings are shown in Figures 15 to 17. The GCEM yields element-wise disconnected crack openings. Both the initiation and the propagation of the cracks are captured. Moreover, not only the major cracks, but also some minor cracks are captured, see the results for $\alpha = 60^\circ$ in Figure 17.

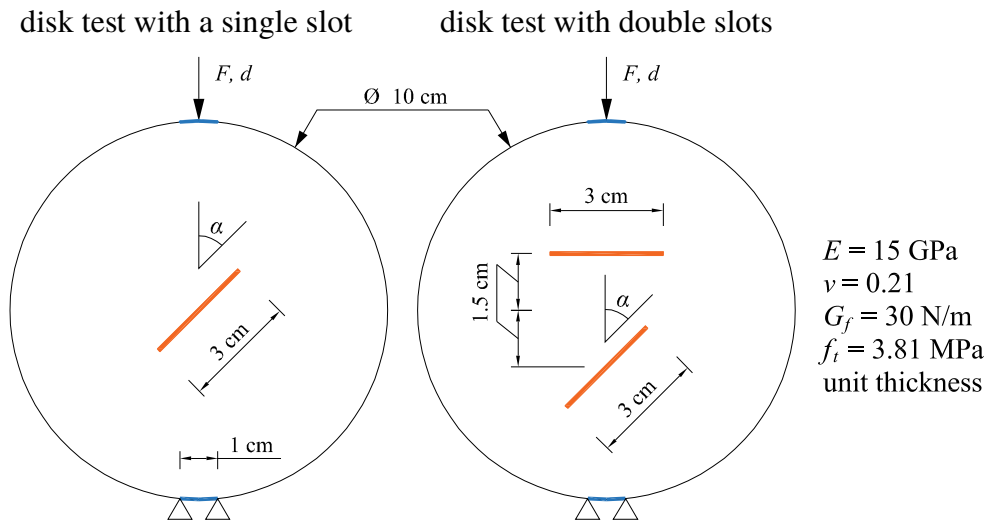


Figure 11: Model of Brazilian disk tests with single or double slots

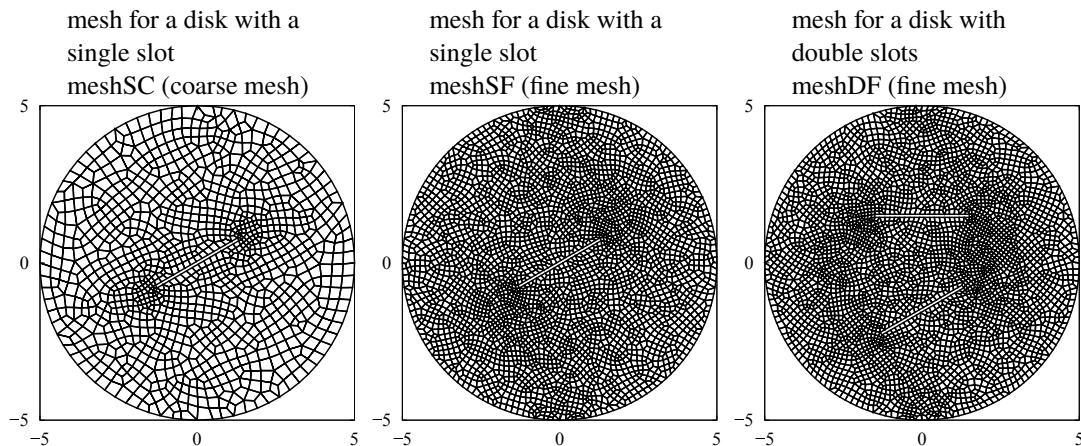


Figure 12: Meshes for Brazilian disk tests with single or double slots (unit: cm)

For disk tests with double slots, force-displacement curves and normalized peak loads are shown in Figure 18. Generally, the latter are similar to the results published in [37].

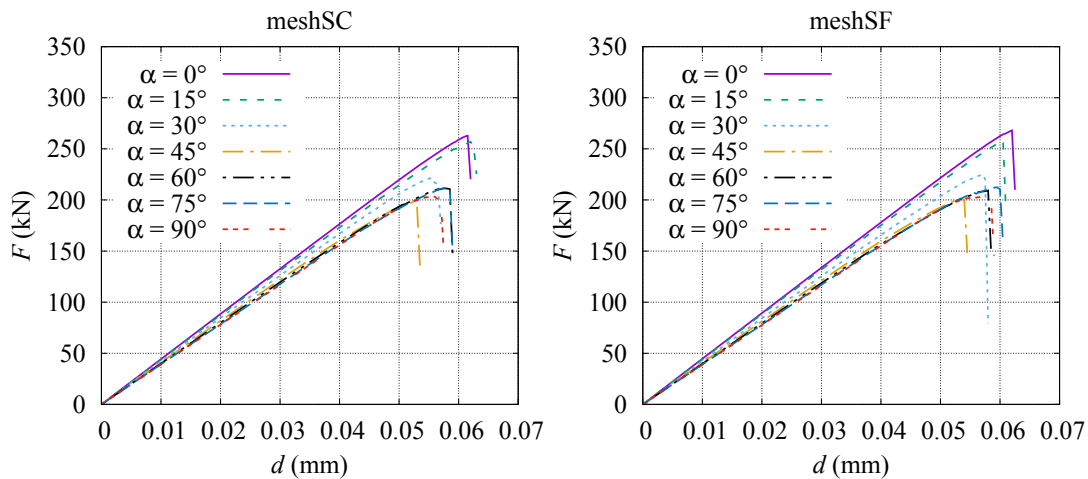


Figure 13: Force-displacement curves of disk tests with a single slot for different meshes

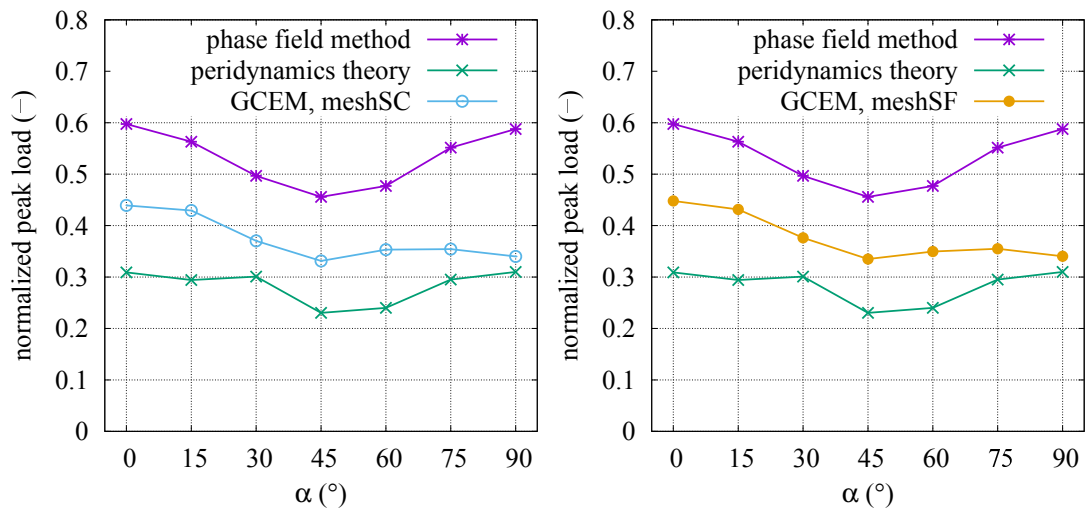


Figure 14: Comparison of normalized peak loads of disk tests with a single slot, for different meshes, with the results published in [37, 38]

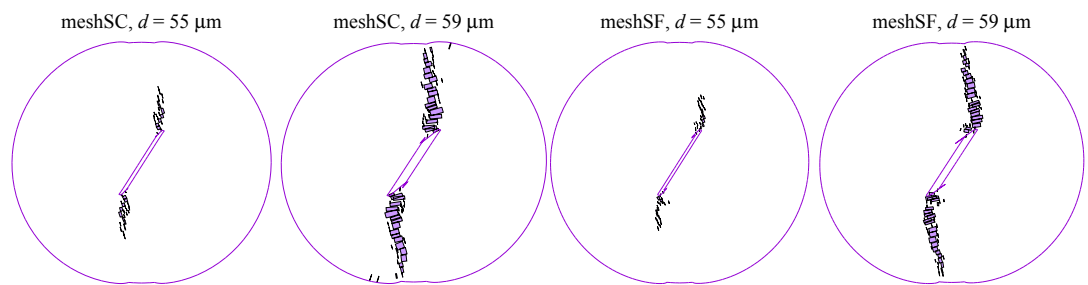


Figure 15: Deformation and crack-opening plots of disk tests with a single slot and $\alpha = 30^\circ$ (scale=1:100)

The results for the crack openings are shown in Figures 19-22, indicating that the GCEM is capable of capturing complex crack growth.

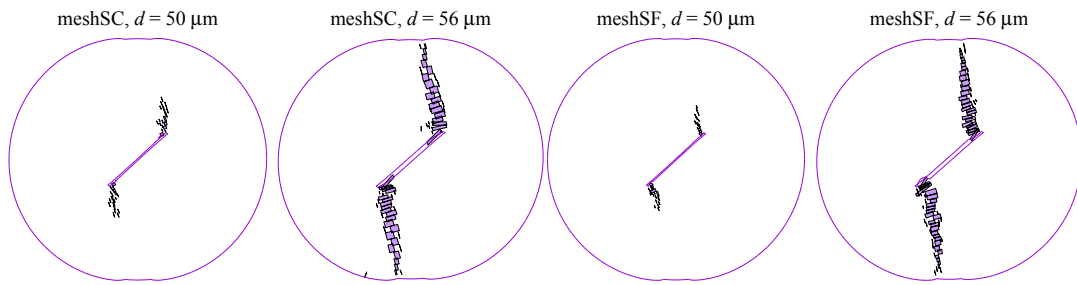


Figure 16: Deformation and crack-opening plots of disk tests with a single slot and $\alpha = 45^\circ$ (scale=1:100)

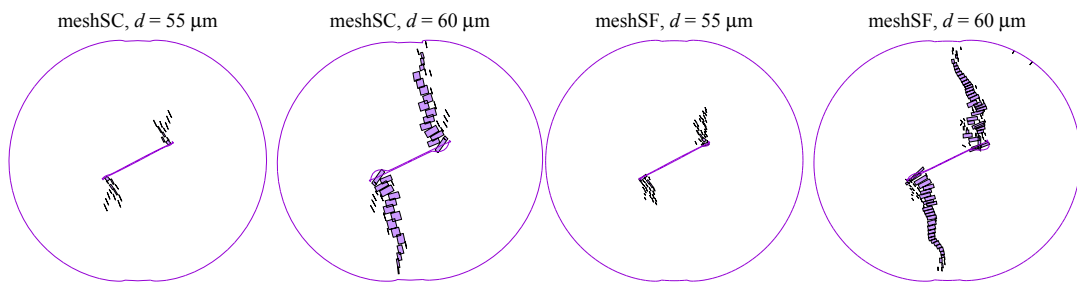


Figure 17: Deformation and crack-opening plots of disk tests with a single slot and $\alpha = 60^\circ$ (scale=1:100)

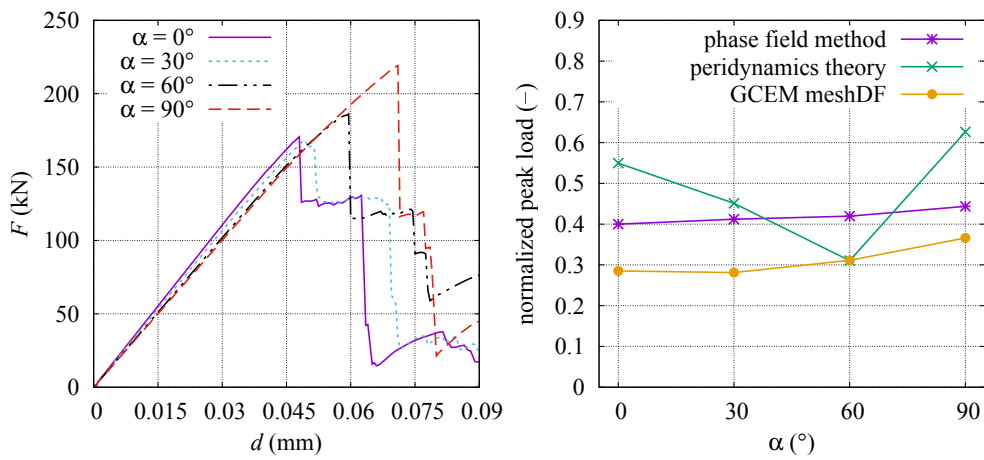


Figure 18: Comparison of results of disk tests with double slots with results reported in [37, 38]: (a) force-displacement curves, (b) normalized peak loads

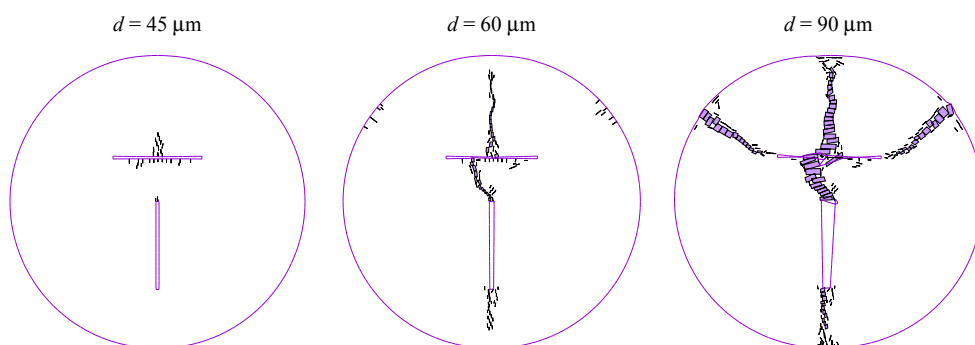


Figure 19: Deformation and crack-opening plots of disk tests with double slots and $\alpha = 0^\circ$ (scale=1:15)

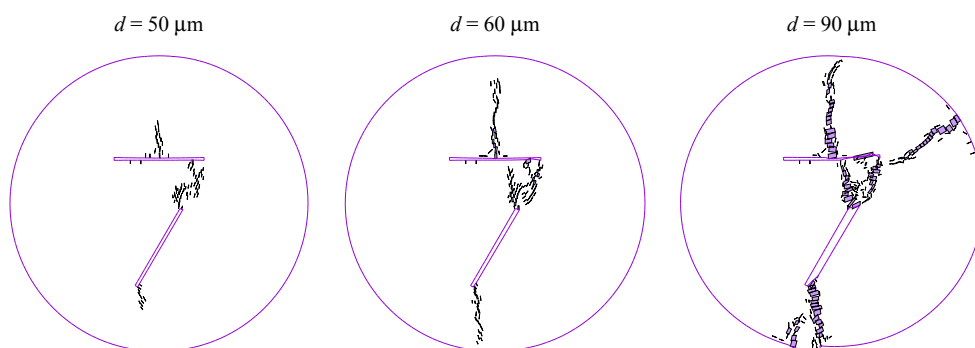


Figure 20: Deformation and crack-opening plots of disk tests with double slots and $\alpha = 30^\circ$ (scale=1:15)

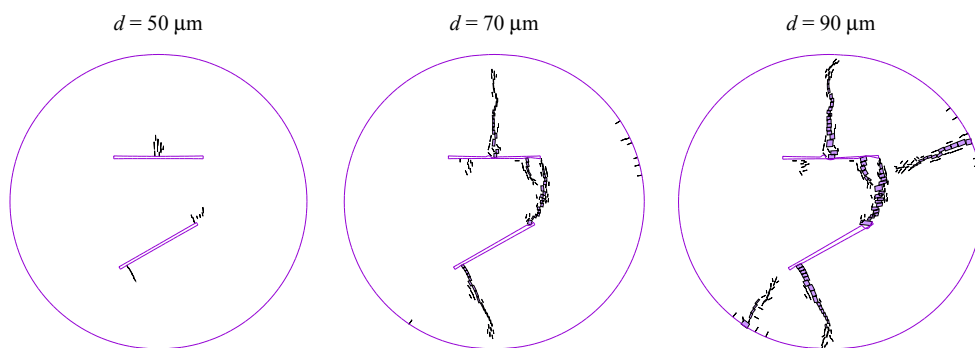


Figure 21: Deformation and crack-opening plots of disk tests with double slots and $\alpha = 60^\circ$ (scale=1:15)

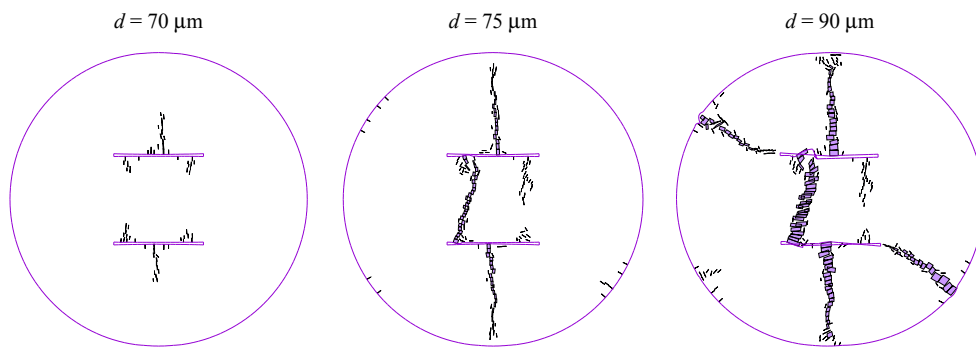


Figure 22: Deformation and crack-opening plots of disk tests with double slots and $\alpha = 90^\circ$ (scale=1:15)

4. CONCLUSIONS

In this paper, following earlier work on the Cracking Elements Method (CEM), a novel standard Galerkin-based numerical approach, named Global Cracking Elements Method (GCEM) was presented. The Global Cracking Elements (GCE) used in the GCEM represent a special type of elements, formally similar to Q9 elements. This feature makes it easy to implement the elements into the FEM. Moreover, unlike the conventional XFEM and SDA, the GCEM does not need nodal/element-wise enrichment or a crack-tracking strategy. Unlike the phase field method, a relatively coarse mesh can be used in the GCEM to obtain reliable results with negligible mesh dependency. Unlike methods based on equivalent-type theories. The GCEM does not introduce bonds/lattices/links and accompanied additional assumptions. It stays in the conventional continuum-based framework. The numerical tests have indicated the reliability, efficiency, and robustness of the GCEM. This method is capable of capturing both the initiation and the propagation of cracks and of obtaining reliable results of mixed-mode crack openings.

One disadvantage of the GCEM is that presently, only quadrilateral elements with nonlinear interpolation of the displacement field can be used. Such elements are obviously more complex than elements with linear interpolation of the displacement field. The other disadvantage of the GCEM is that it avoids and abandons precise descriptions of crack tips. The obtained crack openings are element-wise quantities. Hence, the actual crack tips cannot be tracked directly. Nevertheless, the GCEM is capable of capturing multiple crack growth. This is a very difficult task even for methods that are capable of tracking the actual crack tips.

5. ACKNOWLEDGEMENT

The authors gratefully acknowledge financial support by the National Natural Science Foundation of China (NSFC) (51809069) and by the Hebei Province Natural Science Fund E2019202441.

REFERENCES

- [1] Y. Zhang and X. Zhuang, “Cracking elements: a self-propagating strong discontinuity embedded approach for quasi-brittle fracture,” *Finite Elements in Analysis and Design*, vol. 144, pp. 84–100, 2018.
- [2] Y. Zhang and X. Zhuang, “Cracking elements method for dynamic brittle fracture,” *Theoretical and Applied Fracture Mechanics*, vol. 102, pp. 1–9, 2019.
- [3] R. de Borst, “Some recent issues in computational failure mechanics,” *International Journal for Numerical Methods in Engineering*, vol. 52, pp. 63–95, 2001.
- [4] J.-Y. Wu and M. Cervera, “On the equivalence between traction- and stress-based approaches for the modeling of localized failure in solids,” *Journal of the Mechanics and Physics of Solids*, vol. 82, pp. 137–163, 2015.
- [5] J.-Y. Wu and M. Cervera, “A thermodynamically consistent plastic-damage framework for localized failure in quasi-brittle solids: Material model and strain localization analysis,” *International Journal of Solids and Structures*, vol. 88–89, pp. 227–247, 2016.
- [6] J.-Y. Wu, “A unified phase-field theory for the mechanics of damage and quasi-brittle failure,” *Journal of the Mechanics and Physics of Solids*, vol. 103, pp. 72–99, 2017.
- [7] P. Areias, T. Rabczuk, and D. Dias-da-Costa, “Element-wise fracture algorithm based on rotation of edges,” *Engineering Fracture Mechanics*, vol. 110, pp. 113–137, 2013.
- [8] P. Areias and T. Rabczuk, “Steiner-point free edge cutting of tetrahedral meshes with applications in fracture,” *Finite Elements in Analysis and Design*, vol. 132, pp. 27–41, 2017.
- [9] X. Zhuang, C. Augarde, and K. Mathisen, “Fracture modeling using meshless methods and level sets in 3D: framework and modeling,” *International Journal for Numerical Methods in Engineering*, vol. 92, pp. 969–998, 2012.
- [10] X. Zhuang, C. Augarde, and S. Bordas, “Accurate fracture modelling using meshless methods, the visibility criterion and level sets: Formulation and 2D modelling,”

- International Journal for Numerical Methods in Engineering*, vol. 86, pp. 249–268, 2011.
- [11] T. Rabczuk and G. Zi, “A meshfree method based on the local partition of unity for cohesive cracks,” *Computational Mechanics*, vol. 39, pp. 743–760, 2007.
- [12] S. Silling, “Reformulation of elasticity theory for discontinuities and long-range force,” *Journal of the Mechanics and Physics of Solids*, vol. 48, pp. 175–209, 2000.
- [13] F. Han, G. Lubineau, and Y. Azdoud, “Adaptive coupling between damage mechanics and peridynamics: A route for objective simulation of material degradation up to complete failure,” *Journal of the Mechanics and Physics of Solids*, vol. 94, pp. 453–472, 2016.
- [14] G.-f. Zhao, “Developing a four-dimensional lattice spring model for mechanical responses of solids,” *Computer Methods in Applied Mechanics and Engineering*, vol. 315, pp. 881–895, 2017.
- [15] Y. Zhang, R. Lackner, M. Zeiml, and H. Mang, “Strong discontinuity embedded approach with standard SOS formulation: Element formulation, energy-based crack-tracking strategy, and validations,” *Computer Methods in Applied Mechanics and Engineering*, vol. 287, pp. 335–366, 2015.
- [16] M. Cervera and M. Chiumenti, “Smearred crack approach: back to the original track,” *International Journal for Numerical and Analytical Methods in Geomechanics*, vol. 30, pp. 1173–1199, 2006.
- [17] J. Oliver, I. Dias, and A. Huespe, “Crack-path field and strain-injection techniques in computational modeling of propagating material failure,” *Computer Methods in Applied Mechanics and Engineering*, vol. 274, pp. 289–348, 2014.
- [18] S. Saloustros, L. Pelà, M. Cervera, and P. Roca, “Finite element modelling of internal and multiple localized cracks,” *Computational Mechanics*, vol. 59, pp. 299–316, 2017.
- [19] D. Dias-da-Costa, J. Alfaiate, L. Sluys, P. Areias, and E. Júlio, “An embedded formulation with conforming finite elements to capture strong discontinuities,”

International Journal for Numerical Methods in Engineering, vol. 93, pp. 224–244, 2012.

- [20] C. Miehe, L.-M. Schänzel, and H. Ulmer, “Phase field modeling of fracture in multi-physics problems. Part I. Balance of crack surface and failure criteria for brittle crack propagation in thermo-elastic solids,” *Computer Methods in Applied Mechanics and Engineering*, vol. 294, pp. 449–485, 2015.
- [21] R. de Borst and C. Verhoosel, “Gradient damage vs phase-field approaches for fracture: Similarities and differences,” *Computer Methods in Applied Mechanics and Engineering*, vol. 312, pp. 78–94, 2016.
- [22] J.-H. Song, P. Areias, and T. Belytschko, “A method for dynamic crack and shear band propagation with phantom nodes,” *International Journal for Numerical Methods in Engineering*, vol. 67, pp. 868–893, 2006.
- [23] T. Chau-Dinh, G. Zi, P.-S. Lee, T. Rabczuk, and J.-H. Song, “Phantom-node method for shell models with arbitrary cracks,” *Computers and Structures*, vol. 92-93, pp. 242–246, 2012.
- [24] Z. Wu, L. Ngai, and Y. Wong, “Frictional crack initiation and propagation analysis using the numerical manifold method,” *Computers and Geotechnics*, vol. 39, pp. 38–53, 2012.
- [25] H. Zheng and D. Xu, “New strategies for some issues of numerical manifold method in simulation of crack propagation,” *International Journal for Numerical Methods in Engineering*, vol. 97, pp. 986–1010, 2014.
- [26] Z. Wu, L. Fan, Q. Liu, and G. Ma, “Micro-mechanical modeling of the macro-mechanical response and fracture behavior of rock using the numerical manifold method,” *Engineering Geology*, vol. 225, pp. 49–60, 2017.
- [27] P. Dumstorff and G. Meschke, “Crack propagation criteria in the framework of X-FEM-based structural analyses,” *International Journal for Numerical and Analytical Methods in Geomechanics*, vol. 31, pp. 239–259, 2007.
- [28] S. Saloustros, M. Cervera, and L. Pelà, “Challenges, tools and applications of tracking algorithms in the numerical modelling of cracks in concrete and

- masonry structures,” *Archives of Computational Methods in Engineering*, 2018. doi:10.1007/s11831-018-9274-3.
- [29] T. Belytschko, J. Fish, and B. E. Engelmann, “A Finite element with embedded localization zones,” *Computer Methods in Applied Mechanics and Engineering*, vol. 70, pp. 59–89, 1988.
- [30] G. Meschke and P. Dumstorff, “Energy-based modeling of cohesive and cohesionless cracks via X-FEM,” *Computer Methods in Applied Mechanics and Engineering*, vol. 196, pp. 2338–2357, 2007.
- [31] Y. Zhang and X. Zhuang, “A softening-healing law for self-healing quasi-brittle materials: analyzing with strong discontinuity embedded approach,” *Engineering Fracture Mechanics*, vol. 192, pp. 290–306, 2018.
- [32] J. Mosler and G. Meschke, “3D modelling of strong discontinuities in elastoplastic solids: fixed and rotating localization formulations,” *International Journal for Numerical Methods in Engineering*, vol. 57, pp. 1553–1576, 2003.
- [33] P. Helnwein, “Some remarks on the compressed matrix representation of symmetric second-order and fourth-order tensors,” *Computer Methods in Applied Mechanics and Engineering*, vol. 190, pp. 2753–2770, 2001.
- [34] J.-Y. Wu, F.-B. Li, and S.-L. Xu, “Extended embedded finite elements with continuous displacement jumps for the modeling of localized failure in solids,” *Computer Methods in Applied Mechanics and Engineering*, vol. 285, pp. 346–378, 2015.
- [35] B. Winkler, *Traglastuntersuchungen von unbewehrten und bewehrten Betonstrukturen auf der Grundlage eines objektiven Werkstoffgesetzes für Beton (Ultimate load analysis of plain and reinforced concrete structures based on an objective material law of concrete)*. PhD thesis, University of Innsbruck, 2001.
- [36] H. Haeri, K. Shahriar, M. F. Marji, and P. Moarefvand, “Experimental and numerical study of crack propagation and coalescence in pre-cracked rock-like disks,” *International Journal of Rock Mechanics and Mining Sciences*, vol. 67, pp. 20 – 28, 2014.

- [37] S.-W. Zhou and C.-C. Xia, “Propagation and coalescence of quasi-static cracks in brazilian disks: an insight from a phase field model,” *Acta Geotechnica*, vol. 14, pp. 1195–1214, Aug 2019.
- [38] X.-P. Zhou and Y.-T. Wang, “Numerical simulation of crack propagation and coalescence in pre-cracked rock-like brazilian disks using the non-ordinary state-based peridynamics,” *International Journal of Rock Mechanics and Mining Sciences*, vol. 89, pp. 235 – 249, 2016.
- [39] C. Jiang, G.-F. Zhao, and N. Khalili, “On crack propagation in brittle material using the distinct lattice spring model,” *International Journal of Solids and Structures*, vol. 118-119, pp. 41 – 57, 2017.